ChemComm

ROYAL SOCIETY OF CHEMISTRY

COMMUNICATION

View Article Online
View Journal | View Issue

Check for updates

Cite this: *Chem. Commun.*, 2025, **61**, 6538

Received 11th February 2025,
Accepted 27th March 2025

DOI: 10.1039/d5cc00747j

rsc.li/chemcomm

Anthraquinone substituents modulate ionic hydrogen-bonded organic frameworks to achieve high ionic conductivity for alkali metal ions†

Xu-Yong Chen, Guiqiang Fei,* Xiang-Tian Bai, Simeng Qi, Xiao-Jie Cao, Yi-Da Gao, Xin Luo and Li-Hui Cao *

Herein, we report two charge-assisted hydrogen-bonded organic frameworks (iHOF-24 and iHOF-25) with 3D/2D hydrogen-bonding networks, which exhibit high ionic conductivity for alkali metal ions. Among them, the conductivity of Li^+ is higher than that of Na^+ and K^+, and the ionic conductivities of Li@iHOF-24 and Li@iHOF-25 at 30 °C were 9.44×10^{-5} and 9.85×10^{-5} S cm^{-1}. This change is attributed to the distance between neighboring carbonyl groups in iHOF-24 and iHOF-25, as well as the radius of the loaded alkali metal ions.

Solid-state batteries have received significant attention in the critical area of sustainable energy storage due to their potential advantages in terms of safety, energy density, and cycle life.[1,2] Large-scale, cost-effective production of solid-state batteries requires the development of high-performance solid-state electrolytes.[3,4] Fast ion transport in solid-state electrolytes is critical for solid-state batteries. Currently, most solid-state electrolyte materials are polymers, which exhibit excellent processability, flexibility, and compatibility at the electrolyte/electrolyte interface. However, the limited number of ionic leap sites at room temperature results in low ionic conductivity.[5,6]

To achieve rapid ion transport, a favorable interaction between the ion and the transport site as well as a suitable channel for ion transport are required.[7,8] Porous framework materials have the capacity to facilitate these two factors concurrently. Porous framework materials can increase the number of active sites by adjusting the building blocks while building an ordered pore structure, which promotes the contact between the ions and the material, accelerates ion diffusion and improves ionic conductivity.[9–11] Among several types of porous framework materials, metal–organic frameworks (MOFs),[12,13] covalent organic frameworks (COFs),[14,15] and hydrogen-bonded organic frameworks (HOFs)[16,17] play important roles in scientific and technological applications due to their unique structural features and diverse functions. In the past, MOFs and COFs have been widely used in solid-state electrolytes.[18–22] The abundant porosity and multi-dimensional pore structure in the structure of MOFs and COFs provide uniform distribution and diffusion paths for ion diffusion, effectively lowering the ion diffusion energy barrier and realizing high ionic conductivity.[23–26] HOFs are crystalline framework materials assembled by intermolecular hydrogen-bonding forces, which gives HOFs the unique advantages of mild synthesis, solution processing, and self-repairing ability.[27–30] Shi's team constructed HOFs (NKU-1000)[31] with porous coordination chains as solid electrolytes and used them in lithium–metal batteries, where porous coordination chains with ordered electronegative sites enabled fast and selective Li^+ transport. The solid-state lithium–metal all-cell battery assembled with Li@NKU-1000 as the SSE exhibits a high capacity, superior multiplicative performance, and cycling stability. Xu's group reported the development of high-performance solid-state lithium–oxygen batteries based on a HOF (HOF-DAT) solid-state electrolyte and HOF-DAT@CNT composite anode. By utilizing the abundant dynamic hydrogen-bonding network in the LHOF-DAT framework, they achieved fast Li^+ transport and excellent electrochemical performance.[32] Since HOFs depend on intermolecular hydrogen bonding forces for assembly, weak hydrogen bonding forces may lead to poor stability. Charge-assisted hydrogen bonding, interpenetrating structures, and π–π stacking are effective ways to enhance the stability of framework structures.[29] Prof. Michael Ward has conducted a significant amount of pioneering work on charge-assisted hydrogen bonding framework materials, and Ward's work has shown applications in proton conduction.[33,34]

Herein, two charge-assisted HOFs (**iHOF-24, iHOF-25**) were synthesized by solvent self-assembly of anthraquinone

---

Shaanxi Key Laboratory of Chemical Additives for Industry, College of Chemistry and Chemical Engineering, Shaanxi University of Science and Technology, Xi'an, 710021, China. E-mail: feiguiqiang@sust.edu.cn, caolihui@sust.edu.cn

† Electronic supplementary information (ESI) available: Materials, experimental details, crystal data, crystal structures, IR, thermogravimetric analysis, XPS, ionic conductivity, and ESP maps. CCDC 2334175 and 2334206. For ESI and crystallographic data in CIF or other electronic format see DOI: **https://doi.org/10.1039/d5cc00747j**

disulfonic acid with different substituents and triamino guanidine (TG). **iHOF-24** with 3D hydrogen-bonding networks, and **iHOF-25** with 2D hydrogen-bonding networks are different dimensional hydrogen-bonding networks and thus also exhibit different alkali metal ionic conductivities. The ionic conductivities of **Li@iHOF-24** and **Li@iHOF-25** at 30 °C were 9.44×10^{-5} and 9.85×10^{-5} S cm^{-1}. **iHOF-25** exhibits higher ionic conductivity than **iHOF-24** attributed to the fact that the transport distance of the carbonyl group in the structure of **iHOF-25** is shorter than that of **iHOF-24**, which is favorable for ionic conduction. As the radius of the loading alkali metal ions increases, their ionic conductivity decreases ($Li^+ > Na^+ > K^+$). This is due to the difference in ionic radius, which affects the loading of ions and ion-binding ability. This study shows the potential of HOFs for application with solid-state electrolytes in various battery systems.

iHOF-24 was obtained from the disodium salt of anthraquinone-1,5-disulfonic acid (AQ-1,5-DS) and TG (Fig. 1a) through a solvent evaporation method, resulting in pale yellow needle crystals. Single crystal X-ray diffraction (SC-XRD) analysis showed the molecular formula of **iHOF-24**: $C_{16}H_{24}N_{12}O_8S_2$, structural formula: AQ-1,5-DS$(TG)_2$, which was crystallized in the $P2_1/n$ space group (Table S1, ESI†), and its asymmetric unit was composed of one AQ-1,5-DS^{2-} molecule (Fig. S1a, ESI†), and two TG^+ molecules. The anthraquinone molecules are distributed parallel to the TG molecules, and the anthraquinone molecules and triamino guanidine molecules are each distributed vertically thereby forming a 3D supramolecular structure (Fig. 1b and Fig. S1b, ESI†). Each TG^+ group was connected to four $-SO_3^-$ groups and the carbonyls of two neighboring anthraquinones to form hydrogen bonds, and each $-SO_3^-$ group was connected to five TG^+ groups (Fig. S2, ESI†) to form hydrogen bonds, which results in a three-dimensional hydrogen-bonding network (Fig. S1c and d, ESI†).

iHOF-25 is a colorless needle crystal obtained through a solvent evaporation method from the disodium salt of anthraquinone-2,6-disulfonic acid (AQ-2,6-DS) and TG (Fig. 1a). SC-XRD analysis showed that **iHOF-25** has the molecular formula: $C_{16}H_{24}N_{12}O_8S_2$ and structural formula: AQ-2,6-DS$(TG)_2$, and it crystallizes in the *Pbca* space group (Table S1, ESI†).

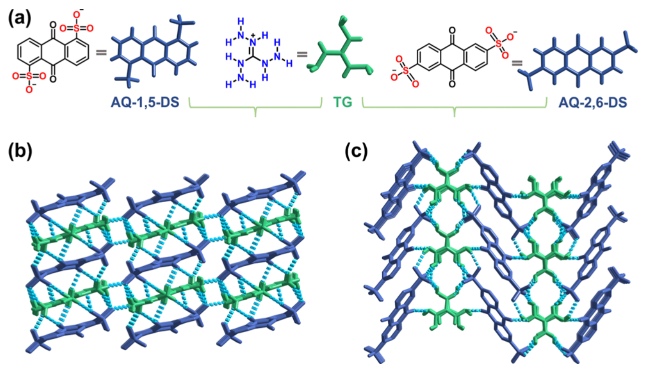

Fig. 1 (a) The **iHOF-24** and **iHOF-25** were prepared through solution self-assembly of AQ-1,5-DS, TG, and AQ-2,6-DS. Supramolecular structure of (b) **iHOF-24**, and (c) **iHOF-25**.

The asymmetric unit of **iHOF-25** consists of an AQ-2,6-DS^{2-} molecule, and two TG^+ molecules (Fig. S3a, ESI†). The anthraquinone molecule and the triamino guanidine molecule are each distributed parallel to each other, forming an anthraquinone plane and a TG plane, and the two planes are distributed parallel to each other to form a supramolecular structure (Fig. 1c and Fig. S3b, ESI†). Each $-SO_3^-$ group is linked to four TG^+ groups to form hydrogen bonds, and each TG^+ group is linked to four $-SO_3^-$ groups (Fig. S4, ESI†) and the carbonyl group to form hydrogen bonds, thus forming a 2D sandwich-shaped hydrogen-bonding network (Fig. S3c, ESI†). The TG acts as a pillar, with the amino group, the carbonyl group, and the sulfonate anion forming a planar hydrogen-bonding network (Fig. S3d, ESI†). Through analysis of the structures, **iHOF-24** and **iHOF-25** are distributed with sulfonate anion groups and carbonyl active sites that facilitate ion transport.

Powder X-ray diffraction (PXRD) of **iHOF-24** and **iHOF-25**, and alkali metal ion-loaded **iHOF-24** and **iHOF-25** (**AM@iHOF-24** and **AM@iHOF-25**) showed the phase purity of **iHOF-24** and **iHOF-25** after synthesis and the framework demonstrated structural integrity after alkali metal ion loading (Fig. 2a and b). The absorption peaks at 3360–3070 cm^{-1} in the infrared spectra (IR) of **iHOF-24** and **iHOF-25** correspond to the stretching vibration bands of the triamino guanidinium cation, water molecules, and hydrogen-bonding in the crystal structure of the **iHOF-24** and **iHOF-25** samples (Fig. S5, ESI†). The absorption peaks in the range of 1574 cm^{-1} and 1660–1702 cm^{-1} are the stretching vibration peaks of the C=O bond and C=N bond. The absorption peaks in the ranges of 1125 cm^{-1}, 1175–1260 cm^{-1} and 600–645 cm^{-1} are the characteristic absorption peaks of $-SO_3^-$ in **iHOF-24** and **iHOF-25.** The synthesis of **iHOF-24** and **iHOF-25** was demonstrated by the analysis of IR combined with PXRD. According to thermogravimetric analysis (Fig. S6, ESI†) of the thermal

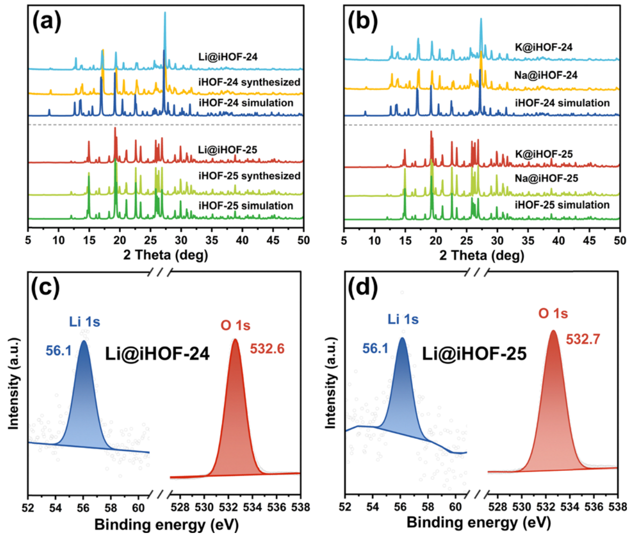

Fig. 2 PXRD patterns of the synthesis of (a) **iHOF-24** and **iHOF-25**, and **Li@iHOF-24** and **Li@iHOF-25**, and (b) PXRD patterns of alkali metal ion loading **iHOF-24** and **iHOF-25**. XPS survey scan of (c) **Li@iHOF-24**, and (d) **Li@iHOF-25**.

stability of **iHOF-24** and **iHOF-25**, the framework of **iHOF-24** and **iHOF-25** remained stable at 183 °C and 250 °C, respectively, and showed good thermal stability. Similarly, we verified the stability of the frameworks before and after the ionic conductivity measurements by PXRD (Fig. S7, ESI†).

Fig. S8 and S9 (ESI†) show the IR spectra of **iHOF-24** and **iHOF-25**, and **AM@iHOF-24** and **AM@iHOF-25** in the wavenumber range of 1600–1800 cm^{-1}. Obviously, the introduction of alkali metal ions induced a change in the C=O position in **AM@iHOF-24** and **AM@iHOF-25**, and the peak representing the C=O functional group weakened when C=O was converted to C=O···Li (Na/K), and the characteristic peak appeared at 1674–1694 cm^{-1}. X-ray photoelectron spectroscopy (XPS) shows the presence of C, N, O, S, Li, Na and K in **AM@iHOF-24** and **AM@iHOF-25**, and the appearance of the XPS signal at 56.1 eV for the Li–O bond verifies the loading of Li (Fig. 2c and d) with loadings of: 3.31% and 3.73% (Fig. S10, ESI†); similarly the appearance of the XPS signals at 1073.3, and 1072.4 eV for Na–O verifies the loading of Na with loadings of: 3.29% and 3.53% (Fig. S11, ESI†); and the appearance of the XPS signals for K–O likewise verified the loading of K with loadings of: 1.97% and 2.16% (Fig. S12, ESI†). XPS combined with IR confirmed the loading of alkali metal ions and PXRD confirmed that the iHOFs retained the framework after loading.

By analyzing the crystal structures of **iHOF-24** and **iHOF-25**, we hypothesize that both the hydrogen-bonding network and the carbonyl group in the structures are effective pathways and sites for ion transport. The ionic conductivities of **Li@iHOF-24** and **Li@iHOF-25** were 9.44×10^{-5} and 9.85×10^{-5} S cm^{-1}, respectively, at 30 °C (Fig. 3a and b). As the temperature increased, the ionic conductivity gradually increased. At 100 °C, the ionic conductivities of **Li@iHOF-24** and **Li@iHOF-25** increased to 5.97×10^{-4} and 6.91×10^{-4} S cm^{-1}. The Li^+ conductivity of **Li@iHOF-25** was 4.3–15.7% higher than **Li@iHOF-24** from 30–100 °C. The ionic conductivities of **AM@iHOF-24** and **AM@iHOF-25** also increase with increasing temperature as the alkali metal ions change (Li^+, Na^+, K^+). Elevated temperatures provide more energy to the ions, facilitating their crossing of the energy barriers and enhancing the transport rate. The ionic conductivities of **Na@iHOF-24** and **Na@iHOF-25** increase from 6.90×10^{-5} and 8.17×10^{-5} S cm^{-1} to 3.96×10^{-4} and 4.83×10^{-4} S cm^{-1}, from 30 to 100 °C (Fig. S13 and S15, ESI†). The ionic conductivities of **K@iHOF-24** and **K@iHOF-25** increase from 6.19×10^{-5} and 6.97×10^{-5} to 2.91×10^{-4} and 4.20×10^{-4} S cm^{-1}, from 30 to 100 °C (Fig. S14 and S15, ESI†). The ionic conductivities of **AM@iHOF-24** and **AM@iHOF-25** gradually increase with increasing temperature and as the radius of the loading ion increases, the enhancement of **iHOF-25** over **iHOF-24** is more pronounced. We also measured the proton conductivity of **iHOF-24** and **iHOF-25** at low humidity conditions (33% RH) (Fig. S16, ESI†), which was 6.52×10^{-8} and 7.14×10^{-7} S cm^{-1}, respectively, at 30 °C, suggesting that proton conduction contributes negligibly to this system.

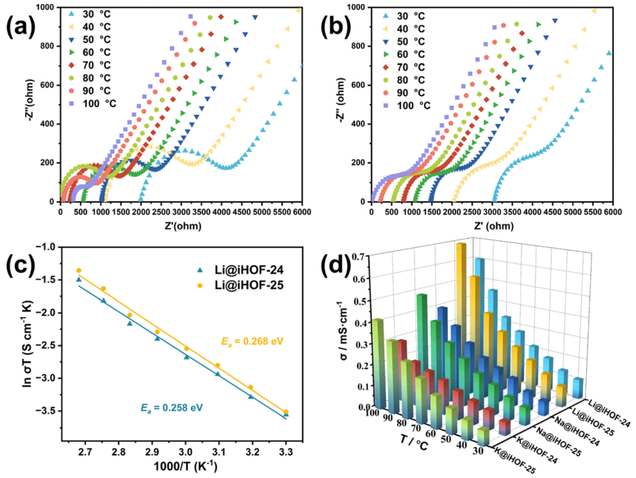

Fig. 3 Nyquist plots of (a) **Li@iHOF-24** and (b) **Li@iHOF-25**, and (c) Arrhenius plots of **Li@iHOF-24** and **Li@iHOF-25**. (d) Ionic conductivity of **Li@iHOF-24**, **Li@iHOF-25**, **Na@iHOF-24**, **Na@iHOF-25**, **K@iHOF-24** and **K@iHOF-25** at 30–100 °C.

Comparing the loading of different alkali metal ions, we found that the ionic radius gradually increased (from Li^+ to Na^+ to K^+) and the ionic conductivities of **AM@iHOF-24** and **AM@iHOF-25** gradually decreased (Fig. 3d), which may be due to the increase of the ionic radius affecting the loading of the ions and the ion-binding ability. In order to further analyze this difference, activation energy (E_a) calculations were carried out, which showed that the E_a values of **AM@iHOF-24** and **AM@iHOF-25** (Fig. 3c and Fig. S13c, S14c, ESI†) are in the lower range of 0.207–0.260 eV, indicating that the alkali metal ions migrate with less energy, resulting in high ionic transport.[31,32] In comparison with solid-state electrolytes based on MOFs and COFs, **iHOF-24** and **iHOF-25** exhibited higher ionic conductivity (Table S2, ESI†). This enhanced performance shows their promising potential for application in advanced solid-state electrolyte systems.

Based on the above analysis and discussion, we propose an ion transport mechanism for **iHOF-24** and **iHOF-25**. In the presence of a 3D/2D hydrogen-bonding network, ions tend to be transported along the hydrogen-bonding network and the active carbonyl site (Fig. 4a and b). The multidimensional paths of 3D networks effectively reduce the ion migration energy barriers, while the directional channels of 2D networks are more favorable for rapid ion transport. In addition, since the neighboring carbonyl distances of the anthraquinone molecule in the **iHOF-25** structure are shorter than those of **iHOF-24**, the shorter distances are favorable for alkali metal ion transport. Therefore, the ionic conductivity (Li^+, Na^+, K^+) of **iHOF-25** is higher than that of **iHOF-24**. To figure out the electronic properties of the **iHOF-24** and **iHOF-25** system, the electrostatic potential (ESP) maps were calculated after stripping zero, one, or two alkali metal cations, respectively (Fig. 4c–e and Fig. S17, S18, ESI†). The nucleophilic regions are shown as blue, and the electrophilic regions are shown as red. The center of the initial structure exhibits a high electron density, which makes it really attracted to alkali metal ions. With the removal of the initial alkali metal ions from the system, the charge distribution

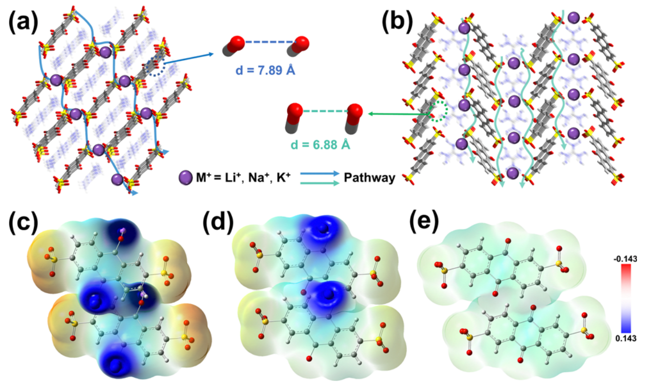

Fig. 4 Ion transport pathways and the distance between carbonyl groups in neighboring anthraquinones of (a) **iHOF-24**, and (b) **iHOF-25**. The ESP maps of **Li@iHOF-25** after stripping (c) zero, (d) one, and (e) two alkali metal ions, respectively.

becomes asymmetric, thereby promoting the detachment of the remaining alkali metal ions, and the center of the molecule slowly changes from being nucleophilic to being electrophilic.[26]

In summary, we have developed **iHOF-24** and **iHOF-25** with 3D/2D hydrogen-bonding networks *via* triamino guanidine and anthraquinone disulfonic acid, resulting in iHOFs with multi-dimensional ionic transport pathways. The ionic conductivities of **Li@iHOF-24** and **Li@iHOF-25** at 30 °C were 9.44×10^{-5} and 9.85×10^{-5} S cm^{-1}, respectively, which increased to 5.97×10^{-4} and 6.91×10^{-4} S cm^{-1}, respectively, at 100 °C. **iHOF-25** exhibits higher ionic conductivity than **iHOF-24** due to the transport distance of the carbonyl group in the structure of **iHOF-25** being shorter than that of **iHOF-24.** As the radius of the loaded ions increases, their ionic conductivity decreases ($Li^+ > Na^+ > K^+$). This is attributable to the disparity in ionic radius, which exerts an influence on the loading of ions and the ion-binding capacity. This verifies the feasibility of constructing ionic conductors with multidimensional ion transport channels and provides guidance for developing various solid-state ionic conductors.

This work was supported by the National Natural Science Foundation of China (22478234, 22075169), the Shaanxi Fundamental Science Research Project for Chemistry and Biology (22JHQ026), and the Shaanxi University of Science and Technology.

Data availability

The data supporting this article have been included as part of the ESI.† Crystallographic data for **iHOF-24** and **iHOF-25** has been deposited at the CCDC under 2334175 and 2334206.†

Conflicts of interest

There are no conflicts to declare.

References

1 J. Zhang, J. Fu, P. Lu, G. Hu, S. Xia, S. Zhang, Z. Wang, Z. Zhou, W. Yan, W. Xia, C. Wang and X. Sun, *Adv. Mater.*, 2025, 2413499.
2 M. Xu, D. Li, Y. Feng, Y. Yuan, Y. Wu, H. Zhao, R. V. Kumar, G. Feng and K. Xi, *Adv. Mater.*, 2024, **36**, 2405079.
3 A. Sood, A. D. Poletayev, D. A. Cogswell, P. M. Csernica, J. T. Mefford, D. Fraggedakis, M. F. Toney, A. M. Lindenberg, M. Z. Bazant and W. C. Chueh, *Nat. Rev. Mater.*, 2021, **6**, 847–867.
4 T. Famprikis, P. Canepa, J. A. Dawson, M. S. Islam and C. Masquelier, *Nat. Mater.*, 2019, **18**, 1278–1291.
5 Y. Kim, C. Li, J. Huang, Y. Yuan, Y. Tian and W. Zhang, *Adv. Mater.*, 2024, **36**, 2407761.
6 X. Zhang, S. Cheng, C. Fu, G. Yin, L. Wang, Y. Wu and H. Huo, *Nano-Micro Lett.*, 2025, **17**, 2.
7 L. Shi, X. Wang and Z. Liu, *Chem. Commun.*, 2024, **60**, 13416–13419.
8 J. Guo, X. Wang, L. Shi and Z. Liu, *Chem. Commun.*, 2025, **61**, 2103–2106.
9 J. Li, X. Jing, Q. Li, S. Li, X. Gao, X. Feng and B. Wang, *Chem. Soc. Rev.*, 2020, **49**, 3565–3604.
10 F. Sheng, B. Wu, X. Li, T. Xu, M. A. Shehzad, X. Wang, L. Ge, H. Wang and T. Xu, *Adv. Mater.*, 2021, **33**, 2104404.
11 D. Guo, D. B. Shinde, W. Shin, E. Abou-Hamad, A.-H. Emwas, Z. Lai and A. Manthiram, *Adv. Mater.*, 2022, **34**, 2201410.
12 H. T. B. Pham, J. Y. Choi, M. Stodolka and J. Park, *Acc. Chem. Res.*, 2024, **57**, 580–589.
13 Q. Wu, J. Liang, D. Wang, R. Wang and C. Janiak, *Chem. Soc. Rev.*, 2025, **54**, 601–622.
14 F. Chen, H. Zheng, Y. Yusran, H. Li, S. Qiu and Q. Fang, *Chem. Soc. Rev.*, 2025, **54**, 484–514.
15 W. Lee, H. Li, Z. Du and D. Feng, *Chem. Soc. Rev.*, 2024, **53**, 8182–8201.
16 A. Ebadi Amooghin, H. Sanaeepur, M. Ghomi, R. Luque, H. Garcia and B. Chen, *Coord. Chem. Rev.*, 2024, **505**, 215660.
17 W. Wei, L. He, G. Han, Y. Lu, S. Shi, Z. Yuan, X. Wang, Y. Li, B. Chen, Z. Zhang and S. Xiang, *Coord. Chem. Rev.*, 2024, **507**, 215760.
18 J. Xue, Z. Sun, B. Sun, C. Zhao, Y. Yang, F. Huo, A. Cabot, H. K. Liu and S. Dou, *ACS Nano*, 2024, **18**, 17439–17468.
19 T. Liu, Y. Zhong, Z. Yan, B. He, T. Liu, Z. Ling, B. Li, X. Liu, J. Zhu, L. Jiang, X. Gao, R. Zhang, J. Zhang, B. Xu and G. Zhang, *Angew. Chem., Int. Ed.*, 2024, **63**, e202411535.
20 H. Wang, W. Huang, R. Rao, J. Zhu, H. Chen, H. Liu, J. Li, Q. Li, M. Bai, X. Wang, X. Wang, T. Liu, K. Amine and Z. Wang, *Adv. Mater.*, 2024, **36**, 2313135.
21 W. Huang, S. Wang, X. Zhang, Y. Kang, H. Zhang, N. Deng, Y. Liang and H. Pang, *Adv. Mater.*, 2023, **35**, 2310147.
22 X.-X. Wang, D.-H. Guan, C.-L. Miao, D.-C. Kong, L.-J. Zheng and J.-J. Xu, *J. Am. Chem. Soc.*, 2023, **145**, 5718–5729.
23 P. Dong, X. Zhang, W. Hiscox, J. Liu, J. Zamora, X. Li, M. Su, Q. Zhang, X. Guo, J. McCloy and M.-K. Song, *Adv. Mater.*, 2023, **35**, 2211841.
24 S. Duan, L. Qian, Y. Zheng, Y. Zhu, X. Liu, L. Dong, W. Yan and J. Zhang, *Adv. Mater.*, 2024, **36**, 2314120.
25 X.-X. Wang, X.-W. Chi, M.-L. Li, D.-H. Guan, C.-L. Miao and J.-J. Xu, *Chem*, 2023, **9**, 394–410.
26 C. Li, D.-D. Wang, G. S. H. Poon Ho, Z. Zhang, J. Huang, K.-T. Bang, C. Y. Lau, S.-Y. Leu, Y. Wang and Y. Kim, *J. Am. Chem. Soc.*, 2023, **145**, 24603–24614.
27 J. Chu, Z. Liu, J. Yu, L. Cheng, H.-G. Wang, F. Cui and G. Zhu, *Angew. Chem., Int. Ed.*, 2024, **63**, e202314411.
28 C. Guo, Y. Gao, S.-Q. Li, Y. Wang, X.-J. Yang, C. Zhi, H. Zhang, Y.-F. Zhu, S. Chen, S.-L. Chou, S.-X. Dou, Y. Xiao and X. Luo, *Adv. Funct. Mater.*, 2024, **34**, 2314851.
29 X.-Y. Chen, L.-H. Cao, X.-T. Bai and X.-J. Cao, *Chem. – Eur. J.*, 2024, **30**, e202303580.
30 X.-J. Cao, L.-H. Cao, X.-T. Bai, X.-Y. Hou and H.-Y. Li, *Adv. Funct. Mater.*, 2024, **34**, 2409359.
31 Z. Han, R. Zhang, J. Jiang, Z. Chen, Y. Ni, W. Xie, J. Xu, Z. Zhou, J. Chen, P. Cheng and W. Shi, *J. Am. Chem. Soc.*, 2023, **145**, 10149–10158.
32 Y. Wang, L.-N. Song, X.-X. Wang, Y.-F. Wang and J.-J. Xu, *Angew. Chem., Int. Ed.*, 2024, **63**, e202401910.
33 T. Adachi and M. D. Ward, *Acc. Chem. Res.*, 2016, **49**, 2669–2679.
34 A. Yusov, A. M. Dillon and M. D. Ward, *Mol. Syst. Des. Eng.*, 2021, **6**, 756.